

Article

Combined PEO and Spray Pyrolysis Coatings of Phosphate and ZnO for Enhancing Corrosion Resistance in AZ31 Mg Alloy

Ashish Kumar Singh ^{1,*}, Reinis Drunka ^{1,2}, Paula Iesalniece ^{1,2}, Ilmars Blumbergs ³, Ints Steins ^{1,2}, Toms-Valdemars Eiduks ², Mairis Iesalnieks ² and Konstantins Savkovs ^{1,3}

- ¹ SMW Group, Kr. Barona Street 3-1, 1050 Riga, Latvia; reinis.drunka@rtu.lv (R.D.); paula.iesalniece@rtu.lv (P.I.); ints.steins@rtu.lv (I.S.); konstantins.savkovs@rtu.lv (K.S.)
² Institute of Materials and Surface Engineering, Faculty of Applied Chemistry and Materials Science, Riga Technical University, Kipsalas Street 6B, 1050 Riga, Latvia; toms-valdemars.eiduks@rtu.lv (T.-V.E.); mairis.iesalnieks@rtu.lv (M.I.)
³ Faculty of Mechanical Engineering, Transport and Aeronautics, Institute of Aeronautics, Riga Technical University, 6B Kipsalas Street Riga, LV-1048 Riga, Latvia, ilmars.blumbergs@rtu.lv
* Correspondence: aksingh@smw.com; Tel.: +371-20587681

Abstract: Oxide films produced from plasma electrolytic oxidation are porous in structure. While they have some passivating effect in Mg alloys, the pores still lead to corrosion over long periods of exposure. In this study, spray pyrolysis was used to seal the porous oxide layer developed through the plasma electrolytic oxidation method on Mg alloy AZ31. The PEO coating acted as a good base for the application of spray pyrolysis due to its morphology. Three different kinds of coatings were obtained using different precursors: zinc acetate for ZnO, phosphoric acid for phosphate (P), and a mixture of zinc acetate and sodium phosphate for ZnO+P. The corrosion performance of all three coatings was studied by performing electrochemical impedance and polarization tests on the samples. Mass loss over a duration of 1 week was measured in 3% NaCl solution using immersion gravimetry. The coating with only phosphate (P) was found to be most corrosion-resistant with 52 times lower rate of corrosion and 50 times more polarization potential. The chemical composition of the corrosion products was studied using XRD and SEM-EDS analysis. Mass loss in ZnO+P was the highest, at up to 1.4 and 5.1 times higher than ZnO and P, respectively.

Keywords: magnesium alloy; ZnO–MgO; electrochemical impedance spectroscopy; spray pyrolysis; potentiodynamic polarization



Citation: Singh, A.K.; Drunka, R.; Iesalniece, P.; Blumbergs, I.; Steins, I.; Eiduks, T.-V.; Iesalnieks, M.; Savkovs, K. Combined PEO and Spray Pyrolysis Coatings of Phosphate and ZnO for Enhancing Corrosion Resistance in AZ31 Mg Alloy. *Surfaces* **2023**, *6*, 364–379. <https://doi.org/10.3390/surfaces6040026>

Academic Editor: Gaetano Granozzi

Received: 17 August 2023
Revised: 22 September 2023
Accepted: 1 October 2023
Published: 10 October 2023



Copyright: © 2023 by the authors. Licensee MDPI, Basel, Switzerland. This article is an open access article distributed under the terms and conditions of the Creative Commons Attribution (CC BY) license (<https://creativecommons.org/licenses/by/4.0/>).

1. Introduction

Magnesium alloys have unique and highly desirable physical and mechanical properties such as high specific strength, specific stiffness, excellent dimensional stability, good machinability, an excellent magnetic screen, superior damping, high fatigue resistance, and high shock resistance ability [1]. Magnesium alloys are the lightest of all structural metals and up to 75% lighter than steel and 25% lighter than aluminum alloys [2]. However, magnesium is prone to corrosion, and despite the exceptional properties exhibited by magnesium alloys, their adoption as the primary choice for designing structures and components has been slow, and manufacturers have historically been cautious about their use [3]. Traditionally, the development and application of corrosion-resistant coatings on bulk magnesium alloys have been employed to make them suitable for use in various conditions. Chemical conversion methods [4–6] have been extensively used in industry but are limited by electrolytes and their environmental impact.

Plasma electrolytic oxidation (PEO) is a method in which a stable, porous, and uniform layer of oxide is formed on the surface of Mg alloy part using an electrolyte and an electrical power source [7,8]. The process is similar to anodizing but employs comparatively higher voltages and currents. It also has a shorter cycle time and can effectively coat a part in a

fraction of the time needed to anodize. The process is very mature, and the coating can be customized to enhance corrosion resistance by adding chemical modifiers such as Zr, P, Si, and Ce [9–11]. Research shows that various kinds of Mg alloys and compositions can be coated with PEO, and the product exhibits superior corrosion resistance compared to bulk materials [11,12].

While PEO oxide coating is stable and inhibits corrosion, it is porous in structure, and corrosion can still take place although at a relatively slower rate. Harsh service environments can further accelerate corrosion by exposing the base metal to the environment, which can be aqueous or gaseous. It is desirable to close the pores with a top layer that is inert and forms a strong adhesion with the porous oxide layer. The PEO oxide layer acts as a suitable base for application of such a coat which can be a polymer paint [13], a deposition of co-polymer [14], and an epoxy-based coating system [15]. These over-coating systems show good results but are prone to peeling and debonding during service. Zinc phosphate coatings from conversion methods have been shown to be effective in improving corrosion resistance [16] by several orders of magnitude. ZnO nanoparticles have been employed to develop pore sealing coating and nanoparticle reinforced PEO coating for improved corrosion resistance [17–19] in Mg alloys using various electrochemical methods. Phosphate seal coats have been applied on the PEO coating of Mg alloys using the solution immersion method [20–22], but the process requires large amounts of solutions. However, excellent results are produced with these methods.

A new method to close the porous PEO oxide layer is used in this study by employing spray pyrolysis (SP). It is a method used to synthesize thin film coatings from chemical precursors. It can deposit homogenous layers of nanoparticles, composites, oxides, or metals on any surface using a spray gun. Changing the composition of the aqueous precursor solution can easily control the properties of the film and the doping level. Temperatures needed for SP operation are in the range of 200–500 °C, which is moderate enough for Mg alloys. The seminal application of SP was performed by Chamberlain and Skarman [23], who used it to coat solar cells with CdS, and since then SP has been used in various applications to produce films and coats of different materials [24–31].

But there is a lack of studies aimed at using SP-obtained coatings to seal the pores on the surface of PEO coatings. Modified PEO coatings were developed on AZ31 using silicate, phosphate, and zirconium modifiers in a previous study [32]. It was found that the pores in the coating were enabling corrosion, even though at a slower rate. ZnO and phosphate pore sealing coatings have not been deposited with the spray pyrolysis method, and no characterization is present. This study seeks to fill this gap and present an initial investigation into the possibility of the SP method for sealing PEO coatings. Here, SP is used to develop ZnO, phosphate only, and ZnO+P coatings on PEO-coated Mg alloy. The base PEO coating is the same, but the coating over it is changed. The spray time is varied to obtain different coatings, and its effect on the corrosion resistance is measured by performing the saltwater corrosion test and electrochemical corrosion testing.

2. Materials and Methods

Magnesium alloy AZ31 plates (SMW Group, Riga, Levita) were used as substrate. PEO coating was performed as described in an earlier study [32]. NaHPO₄ (Sigma Aldrich) was used as the phosphorus source; zinc acetate (Sigma Aldrich, Wien, Austria) was used as zinc source; H₃PO₄ (Sigma Aldrich) was used as source for phosphorus only coating; deionized water (Adrona Crystal 7 Pure Water purification system) was used for washing spray coated specimen. The precursors were produced by diluting concentrated chemicals to achieve 0.1, 0.1, and 0.01 M solutions of NaHPO₄, zinc acetate, and H₃PO₄, respectively.

Three different types of coatings were obtained using the spray pyrolysis method on the PEO coated specimen. The three types of coatings were labeled A, B, and C. For series A, 100 mL of 0.1 M zinc acetate (ZnAc) stabilized with 5 mL of acetic acid was used as raw material to obtain the ZnO coating. For series B, 100 mL of 0.1 M zinc acetate stabilized with 5 mL of acetic acid and NaHPO₄ was used as raw material to obtain the

ZnO and phosphorus coating. And, for series C, 0.01M H₃PO₄ solution was used to create the phosphorus only coating.

Holmarc Spray pyrolysis system HO-TH04BT was used to coat the porous oxide layer produced with the PEO process and to prepare an extra protective coating for the Mg alloy corrosion protection. The thickness of the coatings was controlled by adjusting the spray time of the pyrolysis jet. The times selected were 1, 2, 5, 10, 20, and 30 min, and the specimens were designated from numbers 1 to 6 for each series. The flow rate of the solution was fixed at 1 mL/min, the lateral speed of the spray axle was 400 mm/min, and the transverse speed at 4 mm/min. Samples were heated on a hot plate up to 200 °C to prepare it for spraying to ensure proper adhesion. After the SP process, specimens were washed with deionized water. They were then dried at 110 °C for 4 h and subsequently calcinated at 200 °C for 12 h. The coating nomenclature and specifications are shown in Table 1.

Table 1. Specimen nomenclature according to spray time and coating material on PEO-coated AZ31 samples.

Coating Material	Spray Time (Minutes)					
	1	2	5	10	20	30
ZnO	A1	A2	A5	A10	A20	A30
ZnO+P	B1	B2	B5	B10	B20	B30
P	C1	C2	C5	C10	C20	C30

Corrosion resistance of the coating was tested using two methods, the immersion gravimetric test and the electrochemical method. To calculate the mass loss in the coatings due to corrosion, tests were conducted on the coated specimen along the same guidelines as mentioned in a previous report [32]. A 3% NaCl solution was used, and the specimens were completely immersed in the solution for 1 week (168 h). This is a widely used test used to assess corrosion performance in the absence of dedicated salt spray testing equipment, and similar methods are reported by several researchers [33–35]. The specimens were scratch-marked in an X shape, and the Mg alloy substrate was exposed to assess the direction of the corrosion and self-healing ability of the coating in the event of coating damage. One decreased but untreated Mg AZ31 specimen was also tested for comparison. The mass of specimens before and after the corrosion test was measured to calculate the mass loss by corrosion. The post-corrosion specimens were dried before measuring the mass.

Electrochemical corrosion testing was performed on a Potentiostat/Galvanostat PG-STAT302N Autolab (Metrohm AG, Riga, Latvia) according to method followed earlier [36]. A sealable measuring cell (RHD Instruments GmbH, Darmstadt, Germany) was used. A coating was used as the working electrode, while the reference electrode was a platinum (Pt) wire, and the auxiliary electrode was a glassy carbon electrode. A 3.5% NaCl solution in water was used as the electrolyte. Tafel analysis was applied to each sample in accordance with ASTM G102-89, and the corrosion rate was specified using the electrochemical frequency modulation method. The electrical circuit modeling and fitting was performed using MEISP v3.0 software (Kumho Chemical Laboratories, Seoul Korea).

Characterization of the morphology and chemical and phase content was carried out using a scanning electron microscope Hitachi S-3000N, equipped with an energy-dispersive X-ray spectroscopy (EDS) Bruker Quantax System XFlash 4010 detector and QUANTAX ESPRIT 1.8.2 software to determine the chemical composition of the samples and X-ray diffractometer Bruker AXS D8 Advance, respectively.

3. Results

The spray-coated PEO specimen is shown in Figure 1 along with a control specimen with no PEO or spray coating on it. The X-shaped scratch mark is visible on the specimen to assess the movement of corrosion and its interaction on the coating–substrate interface.

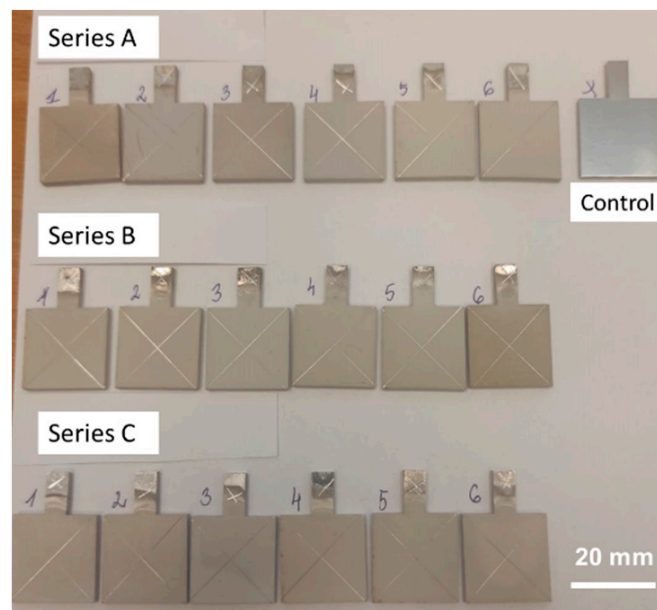


Figure 1. PEO-coated AZ31 specimen treated with spray pyrolysis with a coating of ZnO in series A, ZnO+Phosphorus in series B, and only phosphorus in series C.

3.1. SEM Imaging

Image of the PEO surface is shown in Figure 2a. The pores formed due to a micro arc discharge typical of the PEO process are clearly visible at the surface. For the Mg alloys, the Pilling–Bedford ratio is less than 1 [37], meaning that the density of the coating is less than that of the substrate and is porous without any passivating effect. The surface is rough, with the larger pores on the top and smaller ones lower in the coating. Figure 2b shows the cross-section at an angle of the specimen with both PEO and SP treatments (specimen A6). The pores are filled with the pyrolyzed compounds, and the surface looks sealed. The PEO layer is clearly visible over the substrate and is between 1–3 μm thick. The SP layer was too thin and was not properly resolved to be shown clearly on SEM micrographs.

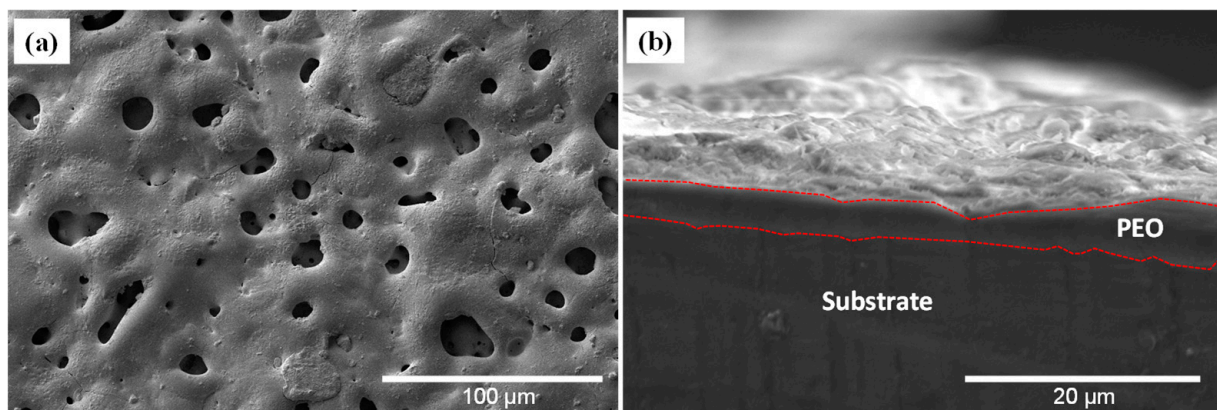


Figure 2. (a) PEO-processed surface of AZ31 and (b) cross-section of PEO sealed with spray pyrolysis.

3.2. XRD Analysis

Figure 3 shows peaks corresponding to Mg, and the 2θ values are consistent with that reported in the literature [33].

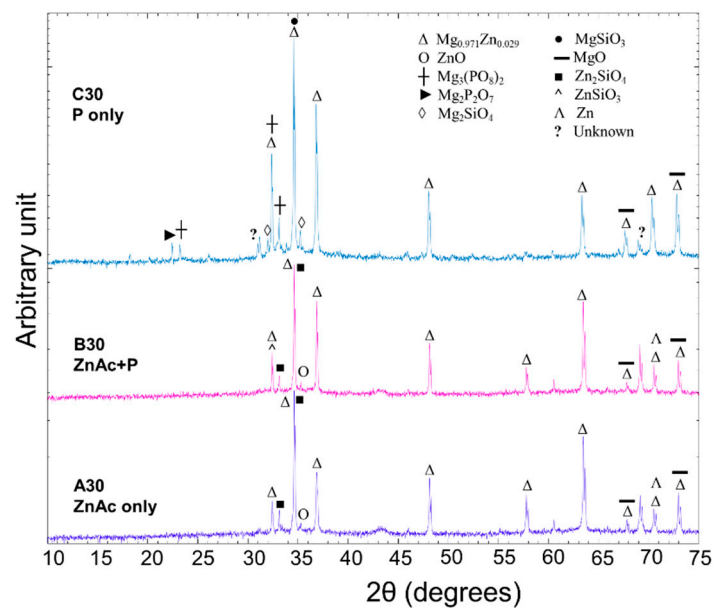


Figure 3. XRD patterns for the SP coatings at 30 min.

In the XRD pattern of the coated specimen shown, the diffraction peaks at 32.32° , 34.56° , 36.78° , 48.04° , 57.65° , 63.38° , 67.66° , 68.98° , 70.36° , and 72.82° are attributed to (100), (101), (102), (2-10), (103), (200), (2-12), (201), and (004) planes of $\text{Mg}_{0.971}\text{Zn}_{0.029}$ phase (COD 00-152-3360), which comes from the substrate. The MgO in the PEO coating is also detected at 67.66° and 72.80° . The substrate structure is typically seen in XRD when the coating is too thin [38], which is applicable in this case as well. Additionally, this can also mean that the SP coating is non-uniform with some porosity.

All three coatings have the $\text{Mg}_{0.971}\text{Zn}_{0.029}$ phase prominently present, with peaks from phases in the coating overlapping them. In the C30 sample (and the entire C series), additional peaks for $\text{Mg}_2\text{P}_2\text{O}_7$ (22.39°), Mg_2SiO_4 (31.91° and 35.26°), and $\text{Mg}_3(\text{PO}_3)_2$ (23.22° , 32.46° , and 33.28°) are also detected, which are formed due to a reaction with the $\text{Mg}_{0.971}\text{Zn}_{0.029}$ phase in the substrate. The absence of the α -Mg phase is the reason for the phosphating in the coating at the spray temperatures used in this study. The presence of phosphates is important in the corrosion resistance of the substrate [16].

The XRD patterns for A30 and B30 were very similar, with the same peaks with different intensities. The ZnO phase at 35.35° attributed to (101) was detected, but no other phase was detected due to the unidirectional growth of the crystals. Weak contributions of peaks from Zn_2SiO_4 and ZnSiO_3 were detected as well. The Si comes from the TEOS used in the PEO electrolyte [32], which reacts with pyrolyzed but unsolidified products of the ZnO. As the thickness grows, some of the ZnO converts to simple Zn due to electron exchange with Mg. No phosphate phase is detected in the B30 specimen, which suggests that no phosphating reaction occurred and that pyrolysis products deposited loosely on the surface.

Since the coatings were not calcined at high temperatures, many phases may not have crystallized and are not shown in the XRD spectrum. Calcination can create polycrystalline dense coatings from SP deposited nanoparticles as shown by Freeman et al. [32]; however, calcination at higher temperatures would also change the mechanical properties of substrate, and this was deemed undesirable in this study.

3.3. Immersion Gravimetric Testing

The spray-coated specimens were tested in a 3% NaCl solution for 1 week using an immersion technique. The corroded samples are shown in Figure 4 along with a control specimen. Visual inspection reveals that the A1, C2, B10, B20, and B30 specimens are most heavily corroded, exhibiting various forms of corrosion damage such as local damage,

discoloration, and bulk corrosion. In series A, the outlier is A1, which experiences the most corrosion. Subsequently, corrosion damage decreases drastically for A2 and increases with processing time. SP produces nanoparticles that deposit on the surface of the PEO coating. The presence of these nanoparticles alters the electrochemistry of the coating and increases corrosion at low nanoparticle concentrations because the pores of the coating are not adequately sealed. A similar effect of the ZnO nanoparticles on the corrosion resistance of the PEO coating was observed by Seyfi et al. [39]. At a low concentration of ZnO, the corrosion resistance was the lowest. As the concentration increased, the corrosion resistance peaked and decreased subsequently.

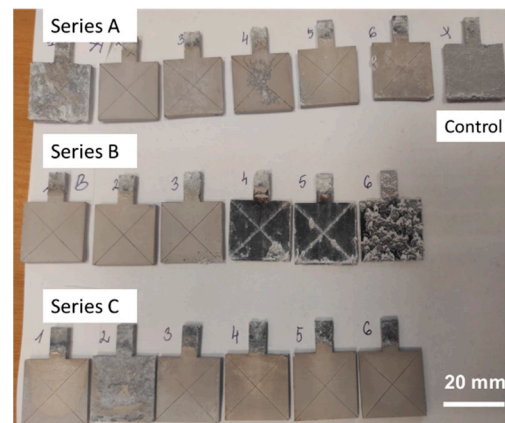
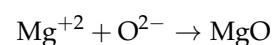
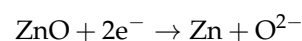
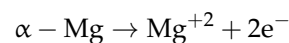


Figure 4. Post-corrosion test specimen of PEO+SP-coated AZ31. The three series A, B, and C are shown, and six specimens with different spray times.

In series A (PEO/ZnO) coatings, the explanation for this behavior is that when the spray time is low, the ZnO coating remains porous and cannot adequately seal the PEO layer. This creates an electrical channel through the open pores between the Mg substrate and ZnO, leading to significant corrosion. The proposed reactions, not in any preferred sequence, are shown below:



For series B (PEO/ZnO+P), an increasing trend in corrosion damage was seen with spray time, although a sudden increase in corrosion was observed at 10 min spray time and beyond. Corrosion damage increased with spray time, and specimens processed at 10 min or more turned black with extensive damage. For series C, a decreasing trend in corrosion with spray time was seen, although C2 is an outlier. Longer spray time improved corrosion resistance only in series C, which means that the pyrolyzed products are good at reducing corrosion.

Results from the immersion gravimetric test (Figure 5) validate the visual observations. The mass loss for the uncoated control AZ31 sample was calculated at 0.97%, which is much more than for all coated samples. The series A does not exhibit a general trend in mass loss, and the images of corroded samples, in Figure 5, also corroborate this result. In specimen A1, the high mass loss compared to the other specimens can be attributed to the formation of numerous ZnO–MgO electrodes at the ZnO nanoparticle deposition site on the MgO coating. It has been shown by Das and Srivastava [40] that such electrode couples have higher electrochemical activity than ZnO. Higher electrochemical activity means that

a higher corrosion current density will be present in the electrode and will lead to higher corrosion [41]. A larger number of electrodes around numerous small and disconnected ZnO nanoparticles that are spread all over the surface causes more uniform corrosion in A1. As the spray time increases (A2 and above), more ZnO is deposited in the pores and surface of the PEO coating, reducing the mass loss due to fewer ZnO–MgO couples.

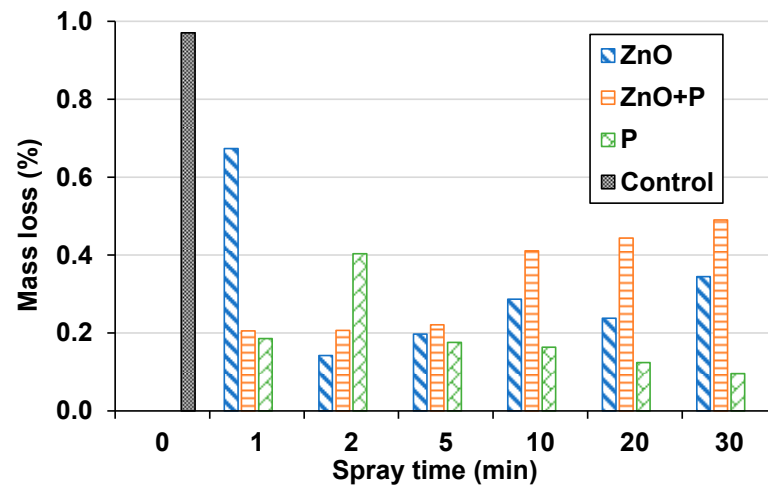


Figure 5. Mass loss for the spray pyrolysis coated AZ31 specimen for various spray times.

The mechanisms of corrosion in PEO-coated Mg alloys have been presented [17]. Therefore, we will focus on the specific case of the corrosion mechanism in the ZnO-containing SP layer on the PEO coating. Figure 6 shows a schematic of the hypothesized mechanism of the ZnO–MgO electrochemical cell formation on PEO/ZnO and PEO/ZnO+P coatings. The schematic illustrates the condition at low spray times (1 or 2 min) where these electrodes are formed at the interfacial area of ZnO–MgO couples. As the spray time increases, this area decreases due to the growth of the ZnO deposition. If no MgO substrate is present next to the ZnO by the corrosive species, the electrode will not have higher activity. But since the SP coating is not able to close the pores of the PEO coating completely, localized corrosion still takes place, as can be seen in Figure 4. Also, since the coating is not calcinated, the coating will not be consolidated and may have intergranular pores. In the case of PEO/ZnO+P, the phosphate groups occupy a large fraction of the available area on the PEO surface, thus reducing the number of these electrodes. This schematic is only intended for explaining the effect of the electrodes and not for explaining the entire corrosion process. While the ZnO pore-sealing coating has been shown to improve corrosion in PEO-coated AZ91 [18], it was possible because the coating thickness was 18.3 μm , and it was able to seal the upper large pores in the PEO coating. In this study, the SP coatings are less than 1 μm thick. Corrosion of the substrate initiates with the diffusion of electrolyte and corrosive ions in the coating. Due to the increased electrochemical activity on the surface of PEO/ZnO and PEO/ZnO+P, especially at lower spray times where the number of electrodes is higher, the diffusion is greater than the PEO/P counterparts. As spray time increases, other factors and mechanisms of corrosion could become dominant for the two ZnO-containing coatings, such as the presence of elemental zinc and the increase in surface roughness induced by the variable deposition and growth of ZnO and phosphates.

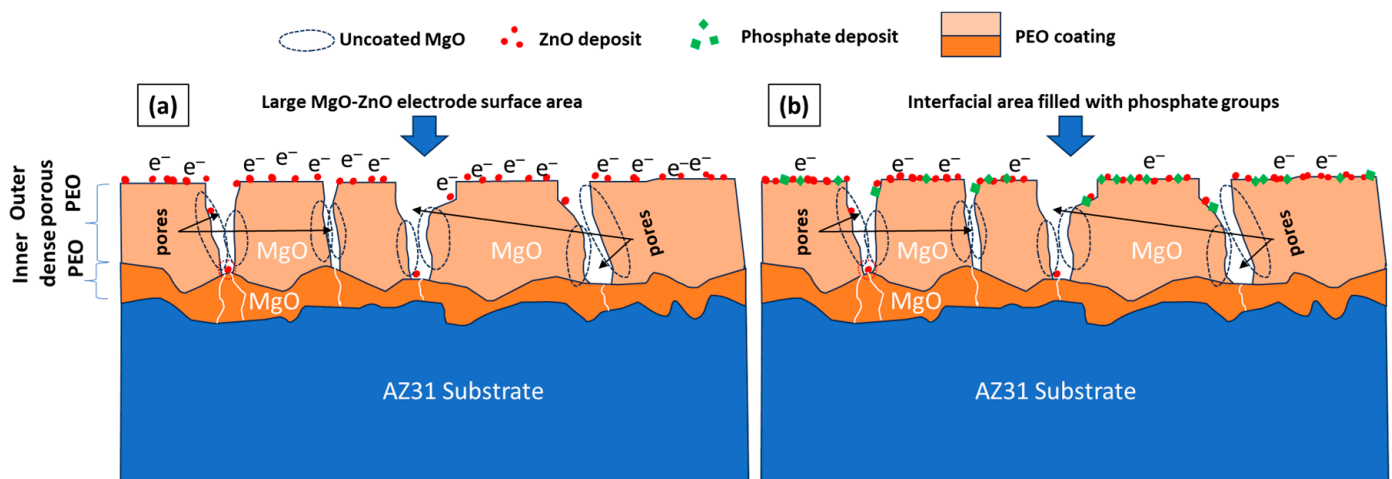


Figure 6. Schematic of corrosion processes in the presence of ZnO particles and formation of its electrochemical couples with MgO in the electrolyte in SP coating with (a) only ZnO and (b) ZnO+P.

The ZnO-pyrolyzed layer deposited using the zinc acetate precursor is more compact and denser compared to other precursors because zinc acetate dissociates and crystallizes before deposition, as described by Lehraki et al. [42]. For other precursors of ZnO, crystallization occurs after deposition, and thermal contraction leads to more porous layers. Here, the ZnO SP layer is more compact and coats the surface more effectively, but some of the hard-to-get regions of the PEO layer are still exposed. These regions, although fewer in number, form larger couples that lead to localized corrosion as opposed to bulk corrosion in A1. Even then, electrode couples still exist, both in the pores and on the surface, and they are larger in size due to the higher ZnO deposition. This leads to more localized corrosion on the surface, and especially around the edges. Also, as more ZnO is deposited, the surface roughness of the coating may increase [43]. Surface roughness and defects play significant roles in the corrosion performance of ceramic coatings [43,44]. So, the increase in mass loss in A2 onward can be explained by the combined effect of stronger localized corrosion on the PEO surface and increasing ZnO corrosion due to surface roughness. As for the A20 specimen, the mass loss is lower than the two adjacent samples and is even corroborated by visual inspection. No conclusive reason could be found for this behavior, and it was assumed to have happened due to a variation in the base PEO-coating properties, or a variation in processing. Even though the SP coating process was kept the same, some variations due to a change in the nozzle or cleaning or changes in the spray chamber after prolonged usage may still occur.

The mass loss in series B specimens shows a clear increasing trend with spray time, as shown in Figure 5. The precursor for this series is a mixture of phosphate- and zinc-containing compounds. It was anticipated that the pyrolysis products would consist of $Zn_3(PO_4)_2 \cdot 4H_2O$, which is shown to improve the corrosion resistance of Mg alloys [16]. But no peaks of $Zn_3(PO_4)_2 \cdot 4H_2O$ were detected in the samples, either due to low content or because it did not form. Even though it can be synthesized at 150 °C [45], a lower temperature than what was used for pyrolysis in this study (200 °C), the spray pyrolysis process does not allow enough time for the reaction to occur properly. Moreover, elemental zinc was detected on the XRD spectrum, which will increase in content as the spray time increases. This means that Zn, ZnO, and other phosphate groups are loosely deposited on the surface and contribute to corrosion. At high spray times, the effect is even more pronounced, and the surface of the SP coating looked so heavily corroded and discolored.

The C series specimens, with only the phosphate coating, have the lowest mass loss for a spray time of 10 min or more, with C30 being the least. The outlier is C2, and in absence of a more comprehensive explanation, the process-related defect formation in the coating is attributed to the increase in mass loss due to corrosion. Two phosphate

groups, $\text{Mg}_2\text{P}_2\text{O}_7$ and $\text{Mg}_3(\text{PO}_8)_2$, are present in the coatings of this series that increase the corrosion resistance of the samples.

3.4. Electrochemical Corrosion Testing

The potentiodynamic polarization curves for the samples are shown in Figure 7. The tests were performed on the samples that displayed the least corrosion damage in each series (A2, B2, C30). Tafel anodic and cathodic processes were used for interpolation at -200 mV to $+100$ mV with respect to the open circuit potential (OCP). Polarization curves provide a measure of the protective properties of any surface, which are characterized by corrosion current density (I_{corr}) and corrosion potential (E_{corr}). It is well known that high corrosion resistance is denoted by increasing E_{corr} and decreasing I_{corr} [16]. But the rate of corrosion is given only by I_{corr} . A higher E_{corr} means that the activation of corrosion will be more difficult but that the corrosion kinetic will be determined by the current density. The intersection of the two slopes was used to obtain corrosion current density and corrosion potential. Current density was multiplied by the area of exposure to obtain the corrosion current. Tafel interpolation was performed, and the parameters are given in Table 2. The current density for AZ31 blank sample is the highest at $1108.8 \mu\text{A}/\text{cm}^2$. This is to be expected since there is no passivating coating on it and corrodes the most. The current density and corrosion potential for C30 (PEO/P) is the least, showing the highest corrosion resistance, followed by PEO/ZnO+P, PEO/ZnO, and AZ31. The current density for the PEO/P coating in this study is less than the $1.66 \mu\text{A}/\text{cm}^2$ produced in a $47 \mu\text{m}$ thick PEO coating in [46]. This shows that the coating is effective compared to even a thick PEO coating.

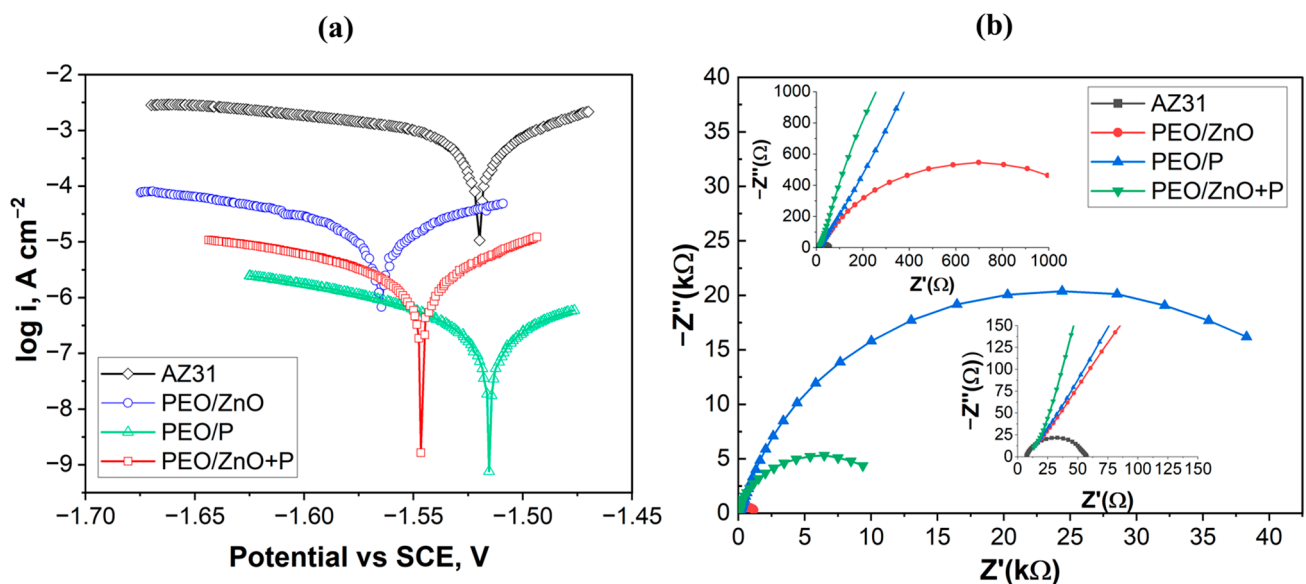


Figure 7. (a) Potentiodynamic polarization (Tafel) curve and (b) electrochemical impedance (Nyquist) curve for the coatings. Insets in (b) show data for different ranges.

From Table 2, the current density for the SP coating with ZnO (A2) and ZnO+P (B2) was 52 and 9 times higher than that for P (C30), respectively, which is the same factor for the corrosion rate since it is linearly related to current density. Low polarization resistance for the A2 sample is indicative of the fact that it is least resistant to oxidation.

In Nyquist plots obtained from impedance measurement, higher corrosion resistance is indicated by the curve with a large radius. The semi-circular capacitive shape is indicative of corrosion under controlled kinetics in the presence of water. An impedance loop with a smaller radius means higher corrosion and a smaller module of impedance. The corrosion resistance of the coatings was corroborated by the Nyquist plots (Figure 7b), where the

radius for the capacitive loop for the samples was in the decreasing order of P, ZnO+P, ZnO, and AZ31.

Table 2. Fit parameters for Tafel analysis of PDP test.

Coating Type	Sample ID	Polarization Resistance Method				
		Corrosion Rate (mm/yr)	I _{corr} (μA/cm ²)	I _{corr} (μA)	Polarization Resistance (kΩ)	E _{corr} (V)
AZ31	Control	50.36	1108.8	1948.5	0.0272	−1.52
ZnO	A2	58.00×10^{-2}	12.7	22.4	1.2	−1.56
ZnO+P	B2	9.71×10^{-2}	2.12	3.76	6.9	−1.55
P	C30	1.11×10^{-2}	0.24	0.43	60.7	−1.52

The Bode plots for the samples along with the fitted curve and corresponding electrical models are shown in Figure 8. The data shows that there is noise and error associated with low frequency data. However, good fit was obtained for all samples. The PEO/ZnO and PEO/ZnO+P coating's EIS response was modeled with the same circuit as shown Figure 8b,d, and a different circuit was used to fit the PEO/P coating. R_{ser} is the uncompensated solution resistance; R_{out} and CPE_{out} are the impedance and constant phase element of the outer SP layer, respectively; CPE_{in} and C_{in} are the constant phase element and capacitance and of the PEO layer, respectively; W_{in} is the Warburg element of the lower dense part of the PEO coating; and R_p is the impedance of the upper porous part of the PEO coating. CPE is a capacitive element with a constant phase deviation from an ideal capacitor. The impedance of CPE is given by $Z_{CPE} = \frac{1}{C(j\omega)^n}$, where $0 < n < 1$. The Warburg element used in the fitting represents finite diffusion with a permeable boundary, and its impedance is given by $Z_O(\omega) = \frac{1}{W_0\sqrt{j\omega}} \tanh(B\sqrt{j\omega})$, where W_0 (Ohm^{−1} s^{−1/2}) is the diffusion-related parameter, and B is given by $B = \delta/\sqrt{D}$, where δ (cm) is the thickness of diffusion layer, and D (cm² s^{−1}) is the diffusion constant [47].

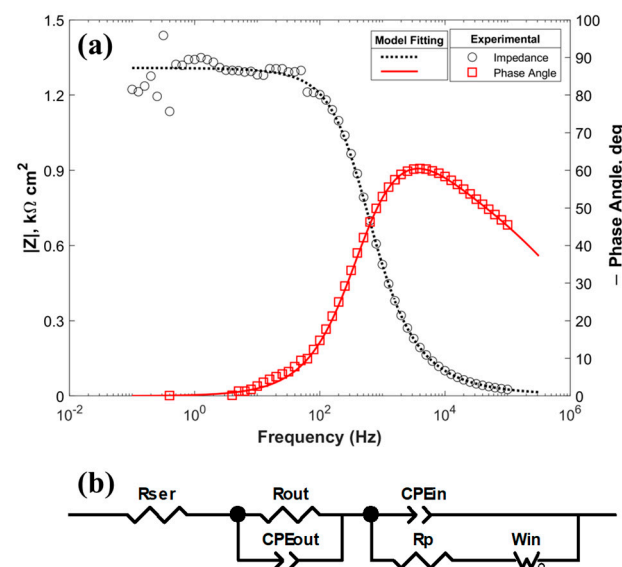


Figure 8. Cont.

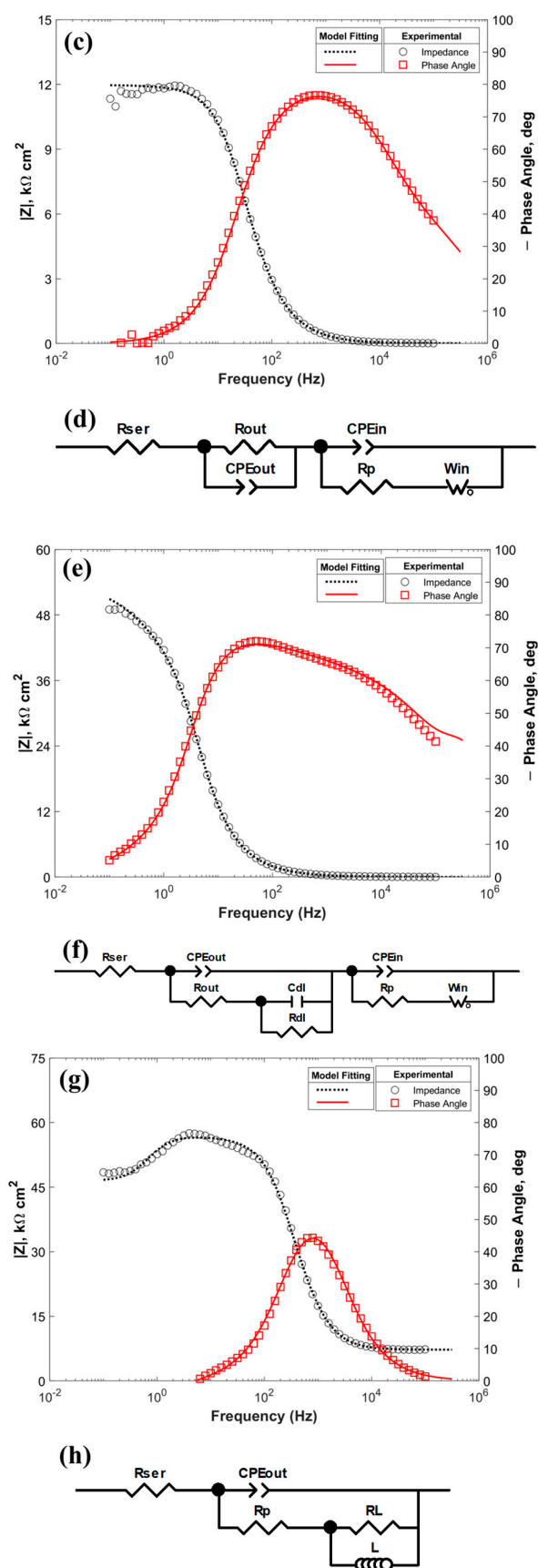


Figure 8. Bode plots and equivalent circuits for (a,b) PEO/ZnO, (c,d) PEO/ZnO+P, (e,f) PEO/P coatings, and (g,h) AZ31 alloy.

All three coatings are represented by two distinct electrical blocks. The equivalent electrical circuits for PEO/ZnO and PEO/ZnO+P have the same configuration: solution resistance, outer SP layer, and inner PEO layer. The block for the PEO has been used widely in the literature to model a passivating layer on metal substrates [17,48,49]. The presence of Warburg elements signifies the presence of a finite diffusion boundary layer between the PEO layer and substrate [47]. There are wide humps at low frequencies in the impedance curve of Bode plots (Figure 8a,c) for PEO/ZnO and PEO/ZnO+P, although the values of impedance are an order of magnitude apart. There is a peak in the phase angle curve of the Bode plots (Figure 8b,d) and a sharp decline after that. A higher peak and longer plateaus in the phase angle generally mean higher impedance in the coating. Meanwhile, for the PEO/P coating, the circuit consists of a stronger passivating outer layer and is similar in structure to the PEO layer. The nested parallel configuration of the SP coating element in PEO/P circuit suggests that it is a two-part coating with a porous and a compact part. Since the coating time was 30 min, it can be conceived that as the coating grows in thickness, it becomes more porous, showing that the layers are passivating for short exposures. The R-C configuration of the SP layers in the other two coatings suggests active corrosion and low impedance. The AZ31 alloy surface was modeled as an inductive element with a low-resistance porous layer that is naturally formed as the surface of the alloy oxidizes.

The values of these parameters obtained from fitting the electrical models are listed in Table 3. It can be seen that the resistance of the solution is close for all tests. The resistance R_{out} of the SP layers in PEO/ZnO, PEO/ZnO+P, and PEO/P are 85.9, 17.8, and 26.5, respectively. But the latter has another compact layer that inhibits corrosion even further. The resistances of the porous parts of the PEO layer are several orders of magnitude larger than the SP layers, meaning that corrosion processes are impeded in the porous PEO more than in the SP layer. The former is 14.95, 671.35, and 1038 times larger than the latter in PEO/ZnO, PEO/ZnO+P and PEO/P, respectively. However, it should be noted that the thicknesses of these coatings are not in the same order, and this difference is to be expected. A smaller value of W_0 indicates lower diffusion across the dense layer of PEO. Its value for the three coatings is different, showing that the diffusion characteristic of the dense part of a PEO layer is dependent on the type of material deposited on top of it. This is in line with the hypothesis that the corrosion in coatings containing ZnO is accelerated by driven by the ZnO–MgO couples. Also, the value of parameter B for the Warburg element is highest for PEO/P, which is related to the impedance of a Warburg element.

Table 3. Electrochemical parameters for AZ31- and PEO/SP-coated samples.

Coating	R_{ser} ($\Omega \text{ cm}^2$)	R_{out} ($\Omega \text{ cm}^2$)	CPE_{out}		CPE_{in}		R_p ($\text{k}\Omega \text{ cm}^2$)	Warburg Element (W)		
			$\mu\text{F cm}^{-2} \text{ s}^{n-1}$	n	$(\mu\text{F cm}^{-2} \text{ s}^{n-1})$	n		W_0 ($\Omega^{-1} \text{ cm}^2 \text{ s}^{-1/2}$)	B ($\times 10^3$)	
PEO/ZnO	4.85	85.9	58.6	0.51	0.73	0.89	1.28	125.66	0.86	
PEO/ZnO+P	5.97	17.8	30.8	0.60	0.96	0.90	11.95	47.14	1.88	
PEO/P	R_{ser} ($\Omega \text{ cm}^2$)	R_{out} ($\Omega \text{ cm}^2$)	CPE_{out}		C_{dl} ($\mu\text{F cm}^{-2}$)	R_{dl} ($\Omega \text{ cm}^2$)	C_{in} ($\mu\text{F cm}^{-2}$)	R_p ($\text{k}\Omega \text{ cm}^2$)	Warburg Element (W)	
			$\mu\text{F cm}^{-2} \text{ s}^{n-1}$	n					W_0 ($\Omega^{-1} \text{ cm}^2 \text{ s}^{-1/2}$)	B ($\times 10^3$)
	5.28	26.5	11.5	0.67	0.215	3.38	1.79	27.51	14.4	17.5
AZ31	R_{ser} ($\Omega \text{ cm}^2$)	R_p ($\Omega \text{ cm}^2$)	CPE_{out}		R_L ($\Omega \text{ cm}^2$)	L (H cm^2)				
			$\mu\text{F cm}^{-2} \text{ s}^{n-1}$	n						
	7.23	39.3	25.75	0.90	10.39	2.29				

For the bare AZ31 sample, the pore resistance was much lower than that of any SP-coated samples. The inductive branch of the circuit has a value of 10.39 H cm^2 .

3.5. EDS Element Analysis

SEM EDS images of specimens A2, B2, and C30 are shown in Figure 9. A segment of the X-shaped scratch mark made on the specimen is visible, being most clearly visible for

specimen A2, with only the ZnO spray coating, followed by C30 (P only) and B2 (ZnO+P). Exposed elemental Mg (in the form of pure metal, MgO, Mg(OH)₂, and other Mg products) is more abundant on the surface of specimen B2 compared to A2 and C30. Figure 9d shows the presence of elemental O, P, and Zn more evenly spread on the surface of specimen B2, showing that the surface is protected by phosphate groups and ZnO.

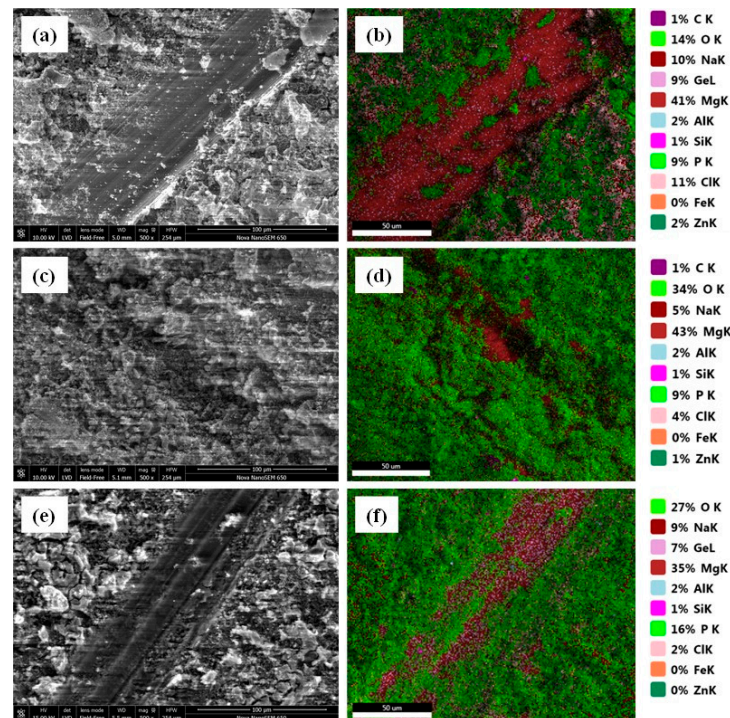


Figure 9. SEM and EDX element overlay map of specimens (a,b) A2, (c,d) B2, and (e,f) C30, respectively.

It also shows that the presence of Mg atoms, whether in alloy form, MgO, or Mg(OH)₂, is lower in the case of C30. It means that both corrosion products and unreacted Mg are not present in the same amount as the other two. The presence of P atoms is much higher and covers even the exposed surface of AZ31. The migration of phosphate groups from the coating moves towards the scratched part, showing signs of self-healing properties of the coating. The effect is also enhanced by the fact that phosphate groups are also present in the PEO coating.

4. Conclusions

Spray pyrolysis on Mg alloy with a PEO oxide layer was performed with three different coating formulations. The pyrolyzed coating was deposited using different spray times, and its effect on the corrosion resistance was studied.

A2, B2, and C30 were most resistant to corrosion in their respective series. The corrosion rate from the PDP test for C30 was 52 and 9 times lower than A2 and B2, respectively.

Spray time had a major impact on the corrosion performance of the SP-coated PEO layer. For series B with ZnO and phosphate coating, longer spray times led to excessive corrosion and discoloration of the surface due to low phosphating and deposition of loosely packed particles.

Series C (only phosphate) showed improved corrosion resistance for spray times longer than 5 min. Migration of phosphate groups to the exposed AZ31 alloy helped in reducing the rate of corrosion. The Mg_{0.971}Zn_{0.029} phase phosphates well produced high corrosion resistance.

The corrosion is dominated by diffusion through a permeable barrier, indicating that the ZnO and ZnO+P coatings do not provide sufficient protection.

The lack of calcination and low pyrolysis temperature does not yield dense and polycrystalline phases in the coating.

Future research will include the growth mechanism of the coatings and the effect of calcination on the coating structure and chemistry. It can be inferred from the results that the chemistry of the coating varies through thickness and leads to inhomogeneities, which leads to corrosion.

Author Contributions: Conceptualization, R.D., I.B., A.K.S., and K.S.; data curation, P.I. and A.K.S.; formal analysis, A.K.S. and R.D.; investigation, P.I., I.S., K.S., T.-V.E., and M.I.; methodology, R.D., A.K.S., I.B., and K.S.; supervision, R.D.; writing—original draft, A.K.S. and R.D.; writing—review and editing, A.K.S. and K.S. All authors have read and agreed to the published version of the manuscript.

Funding: This research was funded by the European Regional Development Fund, grant number CFLA Project 1.1.1.1/19/A/148.

Institutional Review Board Statement: Not applicable.

Informed Consent Statement: Not applicable.

Data Availability Statement: Data is contained within the article.

Acknowledgments: The authors acknowledge RTU for providing the equipment and laboratories for conducting the experiments.

Conflicts of Interest: The authors A.K.S., R.D., P.I., I.S. and K.S. were employed by the company SMW Group, which was the primary applicant and receiver of the funding. The remaining authors declare that the research was conducted in the absence of any commercial or financial relationships that could be construed as a potential conflict of interest. There was no commercial funding for the project.

References

1. Xu, W.; Birbilis, N.; Sha, G.; Wang, Y.; Daniels, J.E.; Xiao, Y.; Ferry, M. A high-specific-strength and corrosion-resistant magnesium alloy. *Nat. Mater.* **2015**, *14*, 1229–1235. [[CrossRef](#)] [[PubMed](#)]
2. Ghassemieh, E. Materials in Automotive Application, State of the Art and Prospects. In *New Trends and Developments in Automotive Industry*; IntechOpen: London, UK, 2011.
3. Kleinbaum, S. Magnesium for Automotive Lightweighting: Status and Challenges. In *Magnesium Technology*; Springer International Publishing: Cham, Switzerland, 2019.
4. Jamali, S.S.; Moulton, S.E.; Tallman, D.E.; Zhao, Y.; Weber, J.; Wallace, G.G. Self-healing characteristic of praseodymium conversion coating on AZNd Mg alloy studied by scanning electrochemical microscopy. *Electrochem. Commun.* **2017**, *76*, 6–9. [[CrossRef](#)]
5. Johari, N.A.; Alias, J.; Zanurin, A.; Mohamed, N.S.; Alang, N.A.; Zain, M.Z.M. Anti-corrosive coatings of magnesium: A review. *Mater. Today Proc.* **2022**, *48*, 1842–1848. [[CrossRef](#)]
6. Yang, K.H.; Ger, M.D.; Hwu, W.H.; Sung, Y.; Liu, Y.C. Study of vanadium-based chemical conversion coating on the corrosion resistance of magnesium alloy. *Mater. Chem. Phys.* **2007**, *101*, 480–485. [[CrossRef](#)]
7. Heydarian, A.; Atapour, M.; Hakimzad, A.; Raeissi, K. The effects of anodic amplitude and waveform of applied voltage on characterization and corrosion performance of the coatings grown by plasma electrolytic oxidation on AZ91 Mg alloy from an aluminate bath. *Surf. Coat. Technol.* **2020**, *383*, 125235. [[CrossRef](#)]
8. Zehra, T.; Fattah-alhosseini, A.; Kaseem, M. Surface properties of plasma electrolytic oxidation coating modified by polymeric materials: A review. *Prog. Org. Coat.* **2022**, *171*, 107053. [[CrossRef](#)]
9. Mashtalyar, D.; Imshinetsky, I.; Sinebryukhov, S.; Gnedenkov, S. Characterization of PEO-Coatings on the MA8 Magnesium Alloy Formed in Electrolyte Containing ZrO₂/SiO₂ Nanoparticles. *Mater. Today Proc.* **2019**, *11*, 134–138. [[CrossRef](#)]
10. Toorani, M.; Aliofkhaezai, M.; Sabour Rouhaghdam, A. Microstructural, protective, inhibitory and semiconducting properties of PEO coatings containing CeO₂ nanoparticles formed on AZ31 Mg alloy. *Surf. Coat. Technol.* **2018**, *352*, 561–580. [[CrossRef](#)]
11. Wang, S.; Xia, Y.; Liu, L.; Si, N. Preparation and performance of MAO coatings obtained on AZ91D Mg alloy under unipolar and bipolar modes in a novel dual electrolyte. *Ceram. Int.* **2014**, *40*, 93–99. [[CrossRef](#)]
12. Zhang, D.; Peng, F.; Qiu, J.; Tan, J.; Zhang, X.; Chen, S.; Qian, S.; Liu, X. Regulating corrosion reactions to enhance the anti-corrosion and self-healing abilities of PEO coating on magnesium. *Corros. Sci.* **2021**, *192*, 109840. [[CrossRef](#)]
13. Mashtalyar, D.; Nadaraia, K.; Sinebryukhov, S.; Gnedenkov, S. Polymer-Containing Layers Formed by PEO and Spray-Coating Method. *Mater. Today Proc.* **2019**, *11*, 150–154. [[CrossRef](#)]
14. Bakhsheshi-Rad, H.R.; Hamzah, E.; Daroonparvar, M.; Abdul Kadir, M.R.; Kasiri-Asgarani, M.; Staiger, M.P. Enhancement of corrosion resistance and mechanical properties of Mg–1.2Ca–2Bi via a hybrid silicon-biopolymer coating system. *Surf. Coat. Technol.* **2016**, *301*, 133–139. [[CrossRef](#)]

15. Wierzbička, E.; Vaghefinazari, B.; Lamaka, S.V.; Zheludkevich, M.L.; Mohedano, M.; Moreno, L.; Visser, P.; Rodriguez, A.; Velasco, J.; Arrabal, R.; et al. Flash-PEO as an alternative to chromate conversion coatings for corrosion protection of Mg alloy. *Corros. Sci.* **2021**, *180*, 109189. [[CrossRef](#)]
16. Yuan, J.; Yuan, R.; Wang, J.; Li, Q.; Xing, X.; Liu, X.; Hu, W. Fabrication and corrosion resistance of phosphate/ZnO multilayer protective coating on magnesium alloy. *Surf. Coat. Technol.* **2018**, *352*, 74–83. [[CrossRef](#)]
17. Bordbar-Khiabani, A.; Yarmand, B.; Mozafari, M. Enhanced corrosion resistance and in-vitro biodegradation of plasma electrolytic oxidation coatings prepared on AZ91 Mg alloy using ZnO nanoparticles-incorporated electrolyte. *Surf. Coat. Technol.* **2019**, *360*, 153–171. [[CrossRef](#)]
18. Bordbar-Khiabani, A.; Yarmand, B.; Mozafari, M. Effect of ZnO pore-sealing layer on anti-corrosion and in-vitro bioactivity behavior of plasma electrolytic oxidized AZ91 magnesium alloy. *Mater. Lett.* **2020**, *258*, 126779. [[CrossRef](#)]
19. Roknian, M.; Fattah-alhosseini, A.; Gashti, S.O.; Keshavarz, M.K. Study of the effect of ZnO nanoparticles addition to PEO coatings on pure titanium substrate: Microstructural analysis, antibacterial effect and corrosion behavior of coatings in Ringer's physiological solution. *J. Alloys Compd.* **2018**, *740*, 330–345. [[CrossRef](#)]
20. Qian, K.; Dong, Q.; Zhang, Y.; Shao, Y.; Cheng, Z.; Xia, D.; Ju, J.; Xue, F.; Chu, C.; Bai, J. Corrosion prevention for PEO-coated Mg by phosphate-based sealing treatment with added cation. *Appl. Surf. Sci.* **2023**, *629*, 157351. [[CrossRef](#)]
21. Qian, K.; Zhang, Y.; Dong, Q.; Shao, Y.; Cheng, Z.; Ju, J.; Xue, F.; Chu, C.; Xia, D.; Bai, J. Enhancement of corrosion resistance and antibacterial properties of PEO coated AZ91D Mg alloy by copper- and phosphate-based sealing treatment. *Corros. Sci.* **2023**, *219*, 111218. [[CrossRef](#)]
22. Phuong, N.V.; Fazal, B.R.; Moon, S. Cerium- and phosphate-based sealing treatments of PEO coated AZ31 Mg alloy. *Surf. Coat. Technol.* **2017**, *309*, 86–95. [[CrossRef](#)]
23. Chamberlin, R.R.; Skarman, J.S. Chemical Spray Deposition Process for Inorganic Films. *J. Electrochem. Soc.* **1966**, *113*, 86. [[CrossRef](#)]
24. Inada, M.; Hojo, J. Synthesis of hollow ceria-zirconia solid solution particles by spray pyrolysis with organic ligands and its oxygen storage capacity. *Adv. Powder Technol.* **2022**, *33*, 103647. [[CrossRef](#)]
25. Nouri, Y.; Hartiti, B.; Labrim, H.; Ziti, A.; Belfhaili, A.; Batan, A.; Fadili, S.; Tahri, M.; Thévenin, P. Synthesis of tin monosulfide SnS thin films via spray pyrolysis method based on Taguchi design for solar absorber. *Opt. Mater.* **2022**, *131*, 112669. [[CrossRef](#)]
26. Hasegawa, H.; Ueda, T.; Yokomori, T. Y2Si2O7:Eu/SiO2 core shell phosphor particles prepared by flame spray pyrolysis. *Proc. Combust. Inst.* **2013**, *34*, 2155–2162. [[CrossRef](#)]
27. Ukoba, K.O.; Eloka-Eboka, A.C.; Inambao, F.L. Review of nanostructured NiO thin film deposition using the spray pyrolysis technique. *Renew. Sustain. Energy Rev.* **2018**, *82*, 2900–2915. [[CrossRef](#)]
28. Hajjar, Z.; Kazemeini, M.; Rashidi, A.; Soltanali, S.; Bahadoran, F. Naphtha HDS over Co-Mo/Graphene catalyst synthesized through the spray pyrolysis technique. *J. Anal. Appl. Pyrolysis* **2017**, *123*, 144–151. [[CrossRef](#)]
29. Annu, A.; Bhattacharya, B.; Singh, P.K.; Shukla, P.K.; Rhee, H.-W. Carbon nanotube using spray pyrolysis: Recent scenario. *J. Alloys Compd.* **2017**, *691*, 970–982. [[CrossRef](#)]
30. Vo, T.K.; Quang, D.T.; Kim, J. Spray pyrolysis-derived MoO3@Al2O3@TiO2 core-shell structures with enhanced hydrodeoxygenation performance. *Catal. Commun.* **2022**, *169*, 106478. [[CrossRef](#)]
31. dos Santos-Gómez, L.; Zamudio-García, J.; Porrás-Vázquez, J.M.; Losilla, E.R.; Marrero-López, D. Recent progress in nanostructured electrodes for solid oxide fuel cells deposited by spray pyrolysis. *J. Power Sources* **2021**, *507*, 230277. [[CrossRef](#)]
32. Drunka, R.; Iesalniece, P.; Savkovs, K.; Krumina, A. Plasma electrolytic oxidation of AZ31 Mg alloy in bipolar pulse mode and influence of corrosion to surface morphology of obtained coatings. *Mat. Sc. (MEDŽIAGOTYRA) early Access.* **2022**. [[CrossRef](#)]
33. Thirumalaikumarasamy, D.; Shanmugam, K.; Balasubramanian, V. Influence of chloride ion concentration on immersion corrosion behaviour of plasma sprayed alumina coatings on AZ31B magnesium alloy. *J. Magnes. Alloys* **2014**, *2*, 325–334. [[CrossRef](#)]
34. Yang, P.; Ye, S.; Feng, B.; Liu, J.; Huang, S.; Liu, G.; Zhang, W.; Tang, W.; Zhu, S.; Zhang, S. Microgalvanic Corrosion of Mg-Ca and Mg-Al-Ca Alloys in NaCl and Na2SO4 Solutions. *Materials* **2021**, *14*, 7140. [[CrossRef](#)] [[PubMed](#)]
35. Pinela, V.M.; de Oliveira, L.A.; de Oliveira, M.C.L.; Antunes, R.A. Study of the Corrosion Process of AZ91D Magnesium Alloy during the First Hours of Immersion in 3.5 wt.% NaCl Solution. *Int. J. Corros.* **2018**, *2018*, 8785154. [[CrossRef](#)]
36. Singh, A.K.; Drunka, R.; Smits, K.; Vanags, M.; Iesalniaks, M.; Joksa, A.A.; Blumbergs, I.; Steins, I. Nanomechanical and Electrochemical Corrosion Testing of Nanocomposite Coating Obtained on AZ31 via Plasma Electrolytic Oxidation Containing TiN and SiC Nanoparticles. *Crystals* **2023**, *13*, 508. [[CrossRef](#)]
37. Xu, C.; Gao, W. Pilling-Bedworth ratio for oxidation of alloys. *Mater. Res. Innov.* **2000**, *3*, 231–235. [[CrossRef](#)]
38. Marzbanrad, B.; Razmpoosh, M.H.; Toyserkani, E.; Jahed, H. Role of heat balance on the microstructure evolution of cold spray coated AZ31B with AA7075. *J. Magnes. Alloys* **2021**, *9*, 1458–1469. [[CrossRef](#)]
39. Seyfi, M.; Fattah-alhosseini, A.; Pajohi-Alamoti, M.; Nikoomanzari, E. Effect of ZnO nanoparticles addition to PEO coatings on AZ31B Mg alloy: Antibacterial effect and corrosion behavior of coatings in Ringer's physiological solution. *J. Asian Ceram. Soc.* **2021**, *9*, 1114–1127. [[CrossRef](#)]
40. Das, S.; Srivasatava, V.C. Synthesis and Characterization of ZnO-MgO Nanocomposite by Co-precipitation Method. *Smart Sci.* **2016**, *4*, 190–195. [[CrossRef](#)]

41. da Silva, R.M.P.; Milagre, M.X.; Izquierdo, J.; Betancor-Abreu, A.M.; de Oliveira, L.A.; Araujo, J.V.d.S.; Antunes, R.A.; Souto, R.M.; Costa, I. Surface finishing effects on the corrosion behavior and electrochemical activity of 2098-T351 aluminum alloy investigated using scanning microelectrochemical techniques. *Mater. Charact.* **2022**, *191*, 112130. [[CrossRef](#)]
42. Lehraki, N.; Aida, M.S.; Abed, S.; Attaf, N.; Attaf, A.; Poulain, M. ZnO thin films deposition by spray pyrolysis: Influence of precursor solution properties. *Curr. Appl. Phys.* **2012**, *12*, 1283–1287. [[CrossRef](#)]
43. Saidi, R.; Raeissi, K.; Ashrafizadeh, F.; Kharaziha, M. The effect of zinc oxide coating morphology on corrosion performance of Ti-6Al-4 V alloys. *J. Alloys Compd.* **2021**, *883*, 160771. [[CrossRef](#)]
44. Perumal, P.; Ramanathan, K.; Ganesan, L.; Subramanian, B.; Ganesh, V.; Stalin, B. Investigation of TiN coating uniformity and its corrosion behaviour using image process. *Mater. Res. Express* **2019**, *6*, 046411. [[CrossRef](#)]
45. Pawlig, O.; Trettin, R. Synthesis and characterization of α -hopeite, $Zn_3(PO_4)_2 \cdot 4H_2O$. *Mater. Res. Bull.* **1999**, *34*, 1959–1966. [[CrossRef](#)]
46. Zhang, Y.; Chen, F.; Zhang, Y.; Du, C. Influence of graphene oxide additive on the tribological and electrochemical corrosion properties of a PEO coating prepared on AZ31 magnesium alloy. *Tribol. Int.* **2020**, *146*, 106135. [[CrossRef](#)]
47. Lazanas, A.C.; Prodromidis, M.I. Electrochemical Impedance Spectroscopy—A Tutorial. *ACS Meas. Sci. Au* **2023**, *3*, 162–193. [[CrossRef](#)]
48. Keyvani, A.; Zamani, M.; Bahamirian, M.; Nikoomanzari, E.; Fattah-alhosseini, A.; Sina, H. Role of incorporation of ZnO nanoparticles on corrosion behavior of ceramic coatings developed on AZ31 magnesium alloy by plasma electrolytic oxidation technique. *Surf. Interfaces* **2021**, *22*, 100728. [[CrossRef](#)]
49. Lou, G.; Jia, P.; Teng, X.; Zhang, J.; Ye, Z.; Wu, H.; Leng, J.; Zuo, M. Nano ZnO-assisted formation of zinc phosphate conversion coating for improving corrosion protection of AZ91D magnesium alloy. *Mater. Res. Express* **2019**, *6*, 086405. [[CrossRef](#)]

Disclaimer/Publisher's Note: The statements, opinions and data contained in all publications are solely those of the individual author(s) and contributor(s) and not of MDPI and/or the editor(s). MDPI and/or the editor(s) disclaim responsibility for any injury to people or property resulting from any ideas, methods, instructions or products referred to in the content.